Temperature distribution during welding measured by neutron imaging

Journal of Physics: Conference Series **2605** (2023) 012026 doi:10.1088/1742-6596/2605/1/012026

Temperature distribution during welding measured by neutron imaging

R. Jamro[1,2,3], T. Mente[4], N. Kardjilov*[1], H. Markötter[4], Ala'A. M. Al-Falahat[5], R. Woracek[6], I. Manke[1] and A. Griesche[4]

[1] Institute of Applied Materials, Helmholtz-Zentrum Berlin für Materialien und Energie, Hahn-Meitner-Platz 1, 14109 Berlin, Germany

[2] Institute of Materials Science and Technology, Technische Universität Berlin, Straße des 17. Juni, 10623 Berlin, Germany

[3] Malaysian Nuclear Agency, 43000 Kajang, Malaysia

[4] Bundesanstalt für Materialforschung und -prüfung (BAM), Unter den Eichen 87, 12205 Berlin, Germany

[5] Department of Mechanical Engineering, Mutah University, Mutah, Al-Karak 61710, Jordan, P.O. Box 7

[6] European Spallation Source ERIC, PO Box 176, Lund 22100, Sweden

*Corresponding author: kardjilov@helmholtz-berlin.de

Abstract: This study was carried out to investigate the neutron transmission signal as a function of sample temperature during a welding process. A theoretical description that includes the Debye-Waller factor was used to describe the temperature influence on the neutron cross-sections. Neutron imaging using a monochromatic beam helps to observe transmission variations related to the material temperature. In-situ neutron imaging of welding experiments show the distribution of the temperature in bulk steel samples. The performed finite element modelling of expected temperature distributions shows good agreement with the obtained experimental data.

Keywords: Debye-Waller factor, in-situ neutron imaging, welding

1. INTRODUCTION

Neutron imaging has become more crucial and popular with humongous scale of applications ranging from materials and energy research to geology application and plant science [1, 2]. In general, the neutron imaging technique is an experimental method for non-destructive investigation of the internal structure of materials or engineering components. It can be applied to a broad range of problems in material research, metallurgical and fundamental sciences [3-6]. Recently, many new neutron imaging techniques and methods had been introduced and developed, which are using different contrast mechanisms, e. g. diffraction, magnetic, phase and dark-field contrast imaging. Especially the Bragg-edge analysis based on energy-selective imaging is gaining more attention because it can provide

essential information on phase distributions in crystalline materials [7-13, 32]. This vital technique exploits variations in the transmitted neutron beam caused by the scattered neutrons due to diffraction from crystal lattice sites. In conjunction to this however, for quantitative data analysis, it is necessary to take into consideration that the diffracted intensity, as well as the inelastically scattered intensity, depends on the temperature of the investigated material. The Debye-Waller factor is typically used to describe the decrease of the elastically diffracted intensity caused by thermal vibrations of atoms at finite temperatures [14-16]. Furthermore, the effect of thermal vibrations of atoms has been observed in the transmission spectrum of cold and thermal neutrons and has been reported several times in the scientific publications [17, 18, 31].

It has been suggested for a while to use "the value of the total cross-section for wavelengths beyond the first Bragg edge to define the temperature of the sample", e.g., by Santisteban [19], while shifts of the Bragg edge position due to thermal expansion were examined as reported by Vogel [9] and Song [20]. Significant attention has been given to exploit the Doppler broadening in neutron resonance absorption imaging (NRAI) [13,21,22] that can be used for remote temperature measurements. Only recently, quantitative experimental strategies were presented and applied to exploit temperature-driven spectral variations of the measured attenuation coefficients in crystalline materials and the effects on the elastic and inelastic scattering cross sections [29,30]. A recent paper by Sato shows the theoretical background for using the temperature dependence of atomic displacement parameter, including the Debye-Waller factor, for measurements of temperature distributions in materials, which we implement in the current paper as well [30].

Here, we present a new technique to investigate in-situ the temperature distribution in a steel sample during welding by neutron imaging. The method is based on energy-selective neutron imaging in the wavelength region, where the thermal motion of atoms causes significant temperature-dependent changes of the neutron transmission. In this work, we measured the two-dimensional neutron transmission through a vertically positioned steel plate sample during remelting of its top side by tungsten inert gas welding. The temperature field underneath the traveling welding torch was simulated by three-dimensional FE modelling as a function of time and compared to the experimentally evaluated results.

2. EXPERIMENT SECTION

The temperature distribution during welding of steel plates was measured by neutron imaging experiments at the Cold Neutron RADiography 2 (CONRAD 2) instrument located at the research reactor BER II of the Helmholtz-Zentrum Berlin für Materialien und Energie. The experimental set-up consists of a remotely-controlled sample holder system allowing for a traverse path of a welding torch along a fixed sample plate. The plate is vertically mounted perpendicular to the neutron flight direction. The distance between plate and scintillator was approximately 10 cm. The scintillator consists of a 200 µm thick ^{6}LiF:ZnS layer. The scintillator converts the transmitted neutrons into visible light, which after mirror reflection by 90°, is recorded with a CCD camera. The magnifying light optic of the camera allowed for a pixel size of 100 µm reflecting in spatial resolution of about 200 µm. A double-crystal monochromator was used to regulate the neutron wavelength in the range between 0.2 nm and 0.6 nm with a resolution of $\Delta\lambda/\lambda \approx 3\%$. The CONRAD 2 instrument is described in detail in [23].

Low transformation temperature (LTT) martensitic steel material was used in these experiments [24]. Sample sheets were made by build-up welding with LTT steel wire and subsequent machining to achieve plates with 100 mm length, 5 mm thickness, and 13 mm height. Figure 1 shows a photo of the set-up. A more detailed description of the samples and the experimental procedure can be found in [25].

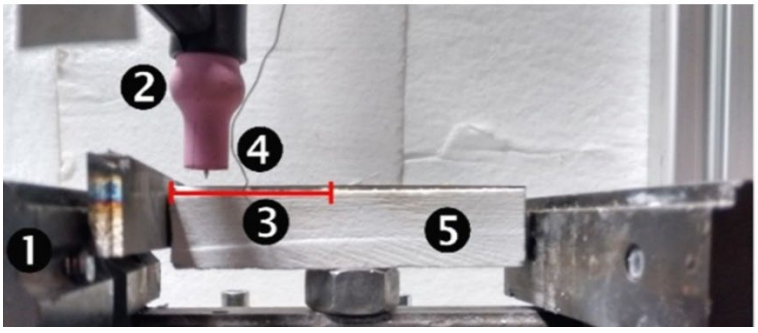

1 Vice to fix the sample
2 Welding nozzle and tungsten electrode
3 Welding length
4 Thermocouple
5 Sample in ceramic insulation

Figure 1: Photo of the welding set-up with the view in neutron flight direction [25]. A parallel clamping device fixes the sample. Alumina felt (white) around the sample reduces thermal losses allowing for longer exposure times. Welding takes place at the narrow side.

The varied parameter for the welding process was the energy input per unit length $E=U*I/v$. E was varied either by changing welding current I or welding velocity v.

Gas tungsten arc welding (GTAW) was used remotly-controlled to weld bead-on-plate with argon as shielding gas. A Castolin CastoTIG 1611 DC power source was used. The welding length for each parameter set was 45 mm, which allowed for four weldments per sample (two on each side, see Figure 1). The used welding parameters were: 60 A welding current and 5 cm / min. welding speed. The used imaging parameters were: neutron wavelength of 0.44 nm and exposure time of 2 s / image.

In a preprocessing step of the image analysis, the acquired images were normalized by background and flat-field corrections, which is a standard procedure in quantitative X-ray and neutron radiography. This way the neutron transmission can be obtained quantitatively.

3. MODELING

To carry out the numerical simulation of the weld thermal cycle and the temperature distribution, a three-dimensional model of the sample was created using the commercial FE program ANSYS®, version 19.2. Figure 2 shows a half of the meshed model. The 3-D element SOLID70 was used to mesh the model with approximately 158000 nodes and 153000 elements in total. The largest element edge length is 0.33 mm and 1.0 mm in the finely and coarsely meshed areas, respectively. The coordinate system originates in the middle of the sample at the centre line of the top surface. The x-axis pointing in longitudinal direction of the sample, which is the welding direction. The y-axis pointing in thickness direction and the z-axis is the height of the sample.

To simulate the moving heat source, nodes in the form of a hemisphere were selected originating from a local coordinate system centred on the top surface of the sample. A temperature of 1540°C was applied to these nodes via a Dirichlet boundary condition [26]. To simulate the movement of the heat source, the local coordinate system was moved along the x-axis as a function of the welding speed. Free convection in air was assumed on all free surfaces of the sample, neglecting the changed heat transfer of the experiment by applying the alumina felt on the sample surface. On the end faces where the specimen was clamped, the nodes were fixed at room temperature. The calculation of the temperature field was based on the thermophysical properties given in [27] for the TX80.

To verify the results, the temperature of the model was compared with the results of the thermocouple of the experiment at the same location, shown in Figure 2 (b). The two thermal cycles of the experiment and the simulation agree very well with only minor deviations.

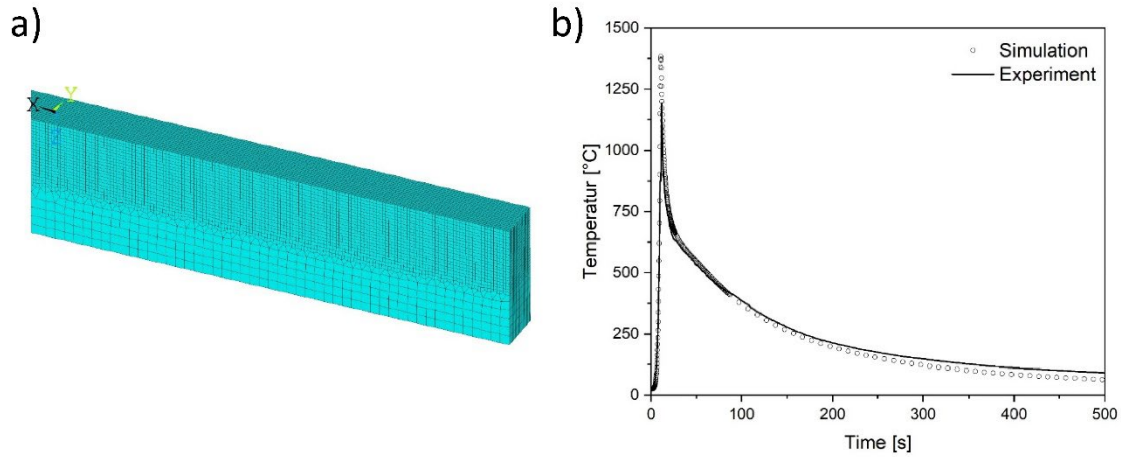

Figure 2: a) Half of the numerical model showing the finely meshed area of interest below the top surface of the model. b) Comparison of the numerically calculated and experimentally recorded temperature at the same location in the sample.

4. RESULTS AND DISCUSSION

A result of the energy-selective investigation of the sample before and after the welding can be seen in Figure 3. From the Figure 3, it's clearly seen that the martensite and austenite material have different attenuation coefficients in the wavelength interval between approximately 0.360 nm and 0.405 nm just below the Bragg-edge wavelengths of both phases respectively. In order to eliminate the effect of phase transformations on the neutron transmission a wavelength above the Bragg-edge was proposed for the measurement. Herein, we present the result of monochromatic imaging during GTAW for visualization of the temperature dependence of the neutron transmission due to – broadly speaking - temperature dependence of atomic displacement parameter in the scattering cross sections.

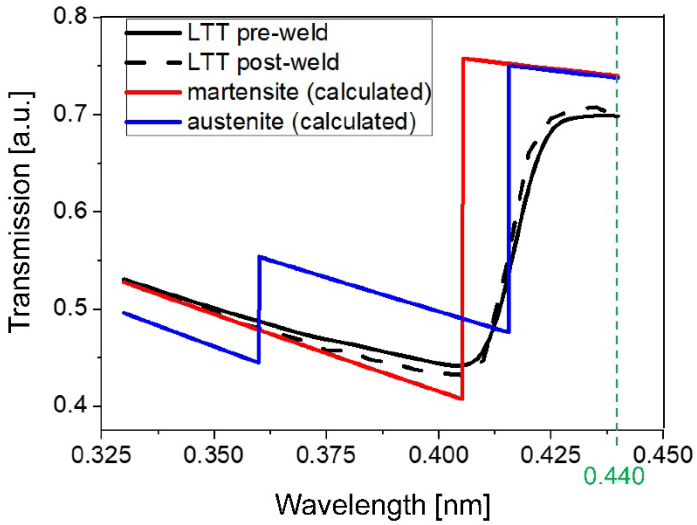

Figure 3: Calculated (blue and red line) and measured (black line) Bragg-edge curves for martensite and austenite at room temperature for a sample thickness of 5 mm. The neutron wavelength of 0.44 nm

used in the transmission experiments is marked with a green dashed line. The theoretical data were calculated with the help of a program library [28].

Meanwhile, Figure 4 (a) reveals the mean value of the transmitted intensity contribution measured just 1 mm underneath from the sample top surface as a function of time marked in the rectangular yellow Region-of-Interest (ROI) shown in the figure.

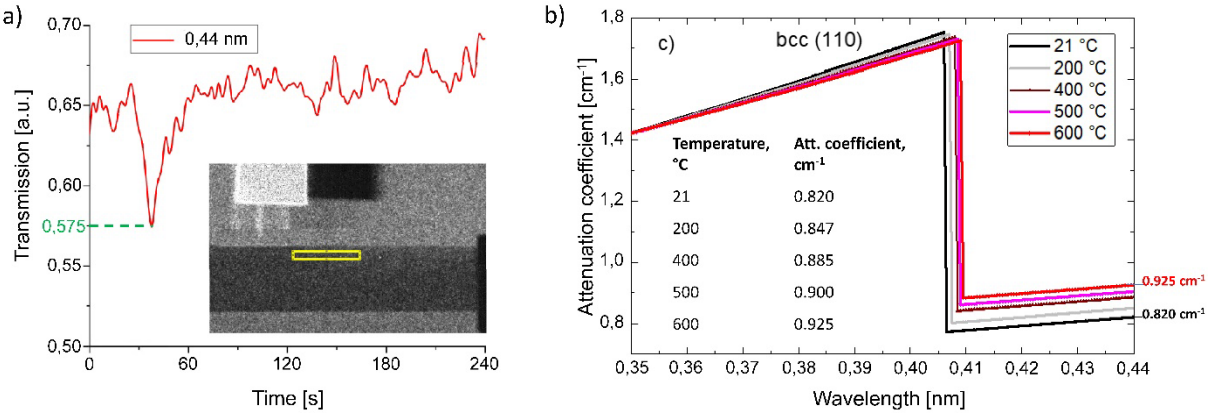

Figure 4: a) Plot of the transmitted intensity measured as the mean value from the ROI (yellow rectangle) as a function of time. The insert shows the monochromatic image taken at t≈130 s. The drop in the intensity in the initial moment of passing of the tip of the torch over the ROI is marked in green. b) Values calculated using the software nxsPlotter [28, 29] for the single b.c.c. (110) phase. The simulations are in good agreement with experimentally determined wavelength dependent attenuation coefficients measured for the given temperatures as shown in [29].

In-situ imaging experiment was performed at a wavelength of 0.44 nm, which is larger than the Bragg-edge wavelengths of both lattice types (martensite and austenite). Therefore, the transmitted intensity should remain constant as shown in Figure 3. Indeed, we observed a drop in intensity by approximately 15% while the welding arc passes the ROI. Subsequently, the measured intensity increases exponentially within approximately 30 s and reaches the initial transmission of approximately 0.66 a.u., which correlates well with the transmission for the martensitic phase as shown in Figure 3.

The observed drop in the transmitted neutron intensity can be explained by the atomic displacement parameter r [29, 30]. The corrections are implemented by the Debye-Waller factor to describe the scattering of neutrons at an oscillating lattice. The immense heat input by the traveling welding arc melts the material at the surface and excites massive lattice oscillations in the subjacent crystalline material. Since the ROI is located 1 mm underneath the surface, most of the material measured should be solid during analysis. These massive lattice oscillations can influence the scattering cross-section for neutrons. This effect of lattice oscillations is commonly considered when using neutron scattering techniques. Until now, this effect was not considered explicitly for neutron imaging. Whether neutrons are scattered with increasing temperature depends on the scattering mechanism. Whereas the elastic neutron cross-section decreases with increasing temperature, the inelastic neutron cross-section increases. Coherent inelastic scattering, however, has the most significant effect and deflects more neutrons at elevated temperatures [29]. Thus, the overall transmitted intensity starts decreasing at high temperatures.

A neutron transmission simulation for the applied LTT steel at different temperatures was performed using the software nxsPlotter and validated experimentally as shown in [29]. From the obtained results presented in Figure 4 (b), it is obvious that the temperature of a sample can be measured by energy-selective neutron radiography using the temperature dependence due to thermal motion of atoms. For

this, a calibration curve using the calculated attenuation coefficients and the corresponding transmission values for different temperatures as shown in Figure 4 (b) was performed. The result is presented in Figure 5 (a).

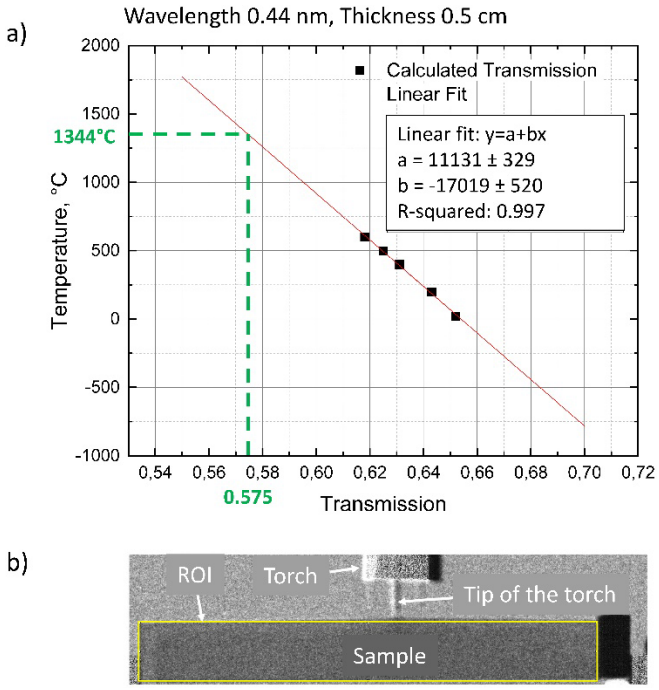

Figure 5: a) Calibration curve of the measured transmission as a function of the temperature for a sample thickness of 5 mm. The evaluation of the temperature at the initial moment of the welding using the transmission drop shown in Figure 4 (a) provides a value of 1344 °C b) The radiograph image of the sample was taken and region of interest (ROI) as highlighted as a yellow rectangle.

The obtained calibration gives us the chance to compare the simulation approach with the experimental data from neutron transmission measurements. The temperature at the initial moment of the welding was estimated from the simulation presented in Figure 2 (b) to be 1375 °C. The transmission value of 0.575 (Fig. 4a) related to this initial moment provides a temperature of 1344 °C using the calibration curve from Figure 5 (a). The temperature values are very close and the difference of 31 K can be explained with the fact that the simulation is calculating the temperature locally in a small volume element of 1 mm^3 in the middle of the sample thickness, while the neutron radiography is an integral method where the measured temperature will be averaged over the sample thickness. This will reflect in lower value of the experimentally determined temperature due to the temperature gradients through the sample thickness as can be seen from Figure 2 (b), where the surface temperature of the sample is measured with a thermal couple to be 1188 K.

The ROI in Figure 5 (b) was selected for further data treatment analysis and the final result was compared with modelling result output. We performed the data analysis by using ImageJ software and plotted with OriginPro. Firstly, 3 images from the data sequence were selected to represent different location of the torch during welding procedure. The image no. 15, image no. 26 and image no. 35 were chosen to represent beginning, middle and end step of the welding process respectively. The images that have been selected were filtered using a nonlinear total variation de-noising filter implemented in ImageJ. After finishing the de-noising analysis, the image was proceed for binning. Basically, binning process is a technique by which signals arriving from adjacent physical elements of an electronic detector are combined to produce a larger pixel/voxel. This increases the signal-to-noise ratio and

provides better contrast resolution, with the trade-off having a reduced spatial resolution. In this experiment, the binning was set to 3x3.

The points of the calibration curve, see Figure 5 (a), were fitted by a linear function y=a+bx, were a= 11131 and b= -17019.

The obtained temperature maps were plotted by OriginPro as shown in Figure 6.

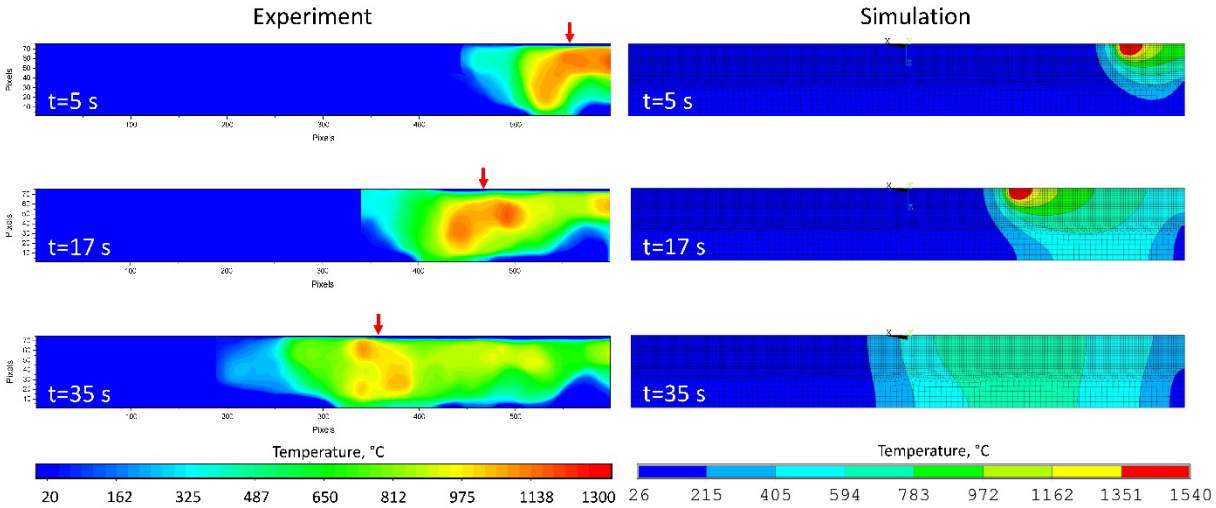

Figure 6: Comparison between experiment and simulation of the temperature distribution during welding (GTAW) of LTT steel plates. The FE model shows just half of the sample.

The agreement between experimental results and simulations in terms of temperature distribution and quantitative temperature levels is very good, which can be used in the future for developing of a quantitative method for determination of temperature fields in dynamic processes like welding, friction, and metal annealing.

5. CONCLUSION

Neutron imaging using a monochromatic beam can be used to observe the influences of thermal effect on the transmission variations spectra on the material samples at the different temperatures. In-situ neutron imaging of welding experiments shows the distribution of the temperature in bulk steel or other polycrystalline samples. The experimentally determined results and the calculated values agree well with the numerical results. The accuracy of the method depends mainly on the neutron statistics and the precise determination of the neutron transmission in short exposure times. The fact that the temperature influences the material attenuation coefficients locally shows the potential for tomography investigations where the temperature distribution and eventually gradients can be studied in 3D maps. This will give an advantage of the demonstrated method in comparison with the standard remote sensing techniques which are used to measure the temperature of distant objects, e.g., instance pyrometric temperature measurements.

ACKNOWLEDGEMENTS

This work was funded by the Helmholtz Gemeinschaft and the Bundesanstalt für Materialforschung und -prüfung (BAM). The authors would also like to thank Jabatan Perkhidmatan Awam (JPA), Government of Malaysia, for financial support.

REFERENCES

[1] Kardjilov N., Manke I., Woracek R., Hilger A. and Banhart J. 2018 *Materials Today*, **21** (6), p 652-672

[2] John Banhart 2008 *Advanced Tomographic Methods in Materials Research and Engineering*. Oxford University Press

[3] Kardjilov N., Hilger A., Manke I., Woracek R., Banhart J. 2016 *J. Appl Crystallogr*, **49**, p 195-202

[4] Strobl M., Manke I., Kardjilov N., Hilger A., Dawson M. and Banhart J. 2009 *Journal of Physics D-Applied Physics*, **42** (24), 243001

[5] Kardjilov N., Manke I., Hilger A., Strobl M. and Banhart J. 2011 *Materials Today*, **14** (6), p 248-256

[6] Eberhard H. L. 2008, *Pramana-J. Phys*., **71,** p 653–661

[7] Meggers K, Priesmeyer H. G, Trela, W. J, Bowman C. D. and Dahms M. 1994 *Nucl. Instrum. Methods Phys. Res. B*., **88**, p 423–429

[8] Steuwer A. and Withers P. J. 2005 *J. Appl. Phys,* **97**, 074903

[9] Vogel S. 2000. PhD thesis, Christian-Albrechts Universität Kiel, Germany

[10] Santisteban J. R., Edwards L., Fitzpatrick M. E, Steuwer A., Withers P. J, Daymond M. R., Johnson M.W., Rhodes N. and Schooneveld E. M. 2002 *Nucl. Instrum. Methods Phys. Res. B,* **481**, p 765–768

[11] Steuwer A., Withers P. J., Santisteban J. R., Edwards L., Bruno G., Fitzpatrick M. E., Daymond M. R., Johnson, M. W. and Wang D. 2001 *Phys. Status Solidi* A, **185**, p 221–230

[12] Woracek R., Santisteban J., Fedrigo A. and Strobl M. 2018 *Nucl. Instrum. Methods Phys. Res. A,* **878**, p 141–158

[13] Sato H. 2018 *J. Imaging,* **4**, 7

[14] James R. W. 1954 *The Optical Principles of the Diffraction of X-rays*. London: G. Bell and Sons

[15] Warren B. E. 1990 *X-ray Diffraction*. New York: Dover Publications

[16] Pecharsky V. K. and Zavalij P. Y. 2009 *Fundamentals of Powder Diffraction and Structural Characterization of Materials*. New York: Springer

[17] Priesmeyer H. G., Stalder M., Vogel S., Meggers K., Bless R. and Trela W. 1999 *Textures Microstruct.*, **33**, p 173–185

[18] Bourke M. A. M., Maldonado J. G., Masters D., Meggers K. and Priesmeyer H. G. 1996 *Mater. Sci. Eng. A*, **221**, p 1–10

[19] Santisteban J. R., Edwards L., Fizpatrick M. E., Steuwer A. and Withers P. J. 2002 *Appl. Phys. Mater. Sci. Process.*, **74**, 1433–1436

[20] Song G., Lin J., Bilheux J., Xie Q., Santodonato L., Molaison J., Skorpenske H. M., Dos Santos A., Tulk C., An K., Stoica A., Kirka M., Dehoff R., Tremsin A., Bunn J., Sochalski-Kolbus L. and Bilheux H. 2017 *J. Imaging*, **3**, 65

[21] Priesmeyer H. G., Stalder M., Vogel S., Meggers K., Bless R. and Trela W. 1999 *Textures Microstruct.*, **33**, p 173–185

[22] Tremsin A. S., Ganguly S., Meco S. M., Pardal G. R., Shinohara T. and Feller W. B 2016 *J. Appl. Cryst.* **49**, p 1130–1140

[23] Kardjilov N., Hilger A., Manke I., Griesche A. and Banhart J. 2015 *Phys. Proc.* **69**, p 60–66

[24] Igwemezie V., Shamir M., Mehmanparast A. and Ganguly S. 2022 *Journal of Advanced Joining Processes* **5** 100110

[25] Griesche A., Pfretzschner B., Taparli U. A. and Nikolay K. 2021 *Applied Sciences* **11** (22)

[26] Lindgren L.-E. 2001 *J. of Thermal Stresses,* **24**, 2, p 141-192

[27] Sun Z. and Yu X. 2002 *J. of Material Research and Technology*, **18**, p 3564-3580

[28] Boin M., 2012 *J. Appl. Cryst*., **45**, p 603-607

[29] Al-Falaha, A. A. M, Kardjiloy N., Woracek R., Boin M., Markötter H., Kuhn L.. T, Makowska M., Strobl M., Pfretzschner B., Banhart J. and Manke I. 2022 *Journal of Applied Crystallography*, **55**(4)

[30] Sato H., Miyoshi M., Ramadhan R. S., Kockelmann W. and Kamiyama T. 2023 *Scientific Reports*, **13**(1), 688

[31] Siegwart M., Woracek R., Marquez Damian J. I., Tremsin A. S., Manzi-Orezzoli V., Strobl M., Schmidt T. J. and Boillat, P. 2019 *Review of Scientific Instruments*, **90**(10), 103705

[32] Tran K. V., Woracek R., Kardjilov N., Markötter H., Hilger A., Kockelmann W., Kelleher J., Puplampu S. B., Penumadu D., Tremsin A. S., Banhart J. and Manke I., 2021 *Materials Today Advances*, **9**, 100132